Hot compaction of nanocrystalline TiO_2 (anatase) ceramics. Mechanisms of densification: Grain size and doping effects

A. Weibel, R. Bouchet, P. Bouvier and P. Knauth

MADIREL (UMR 6121), Université de Provence-CNRS, Centre St Jérôme, 13397 Marseille Cedex 20, France
LEPMI (UMR 5631), Université Joseph Fourier-INPG-CNRS, 38402 St Martin d'Hères Cedex, France

Abstract

The hot compaction of nanocrystalline TiO_2 anatase powders is investigated using dilatometry. The constant rate of heating (CRH) method is applied to determine effective activation energies of the processes involved during sintering. Grain size and doping effects are studied, using dopant cations of different radius and charge: Zn^{2+}, Al^{3+}, Si^{4+}, Nb^{5+}. The results are interpreted by a mechanism including superplastic deformation and boundary diffusion. The former is predominant for small particles and low temperature, whereas the latter is more important for larger particles and higher temperature. Dopant effects on densification kinetics are discussed in view of defect chemistry.

Keywords: Dilatometry; Sintering; Diffusion; Superplastic deformation; Defect chemistry

1. Introduction

In recent years nanostructured materials have attracted increasing attention from the scientific community. The reason for this interest is their unusual physical properties, which open up possibilities for new technological applications, such as in electronics, catalysis, magnetic data storage, energy storage, structural components and ceramics [1]. Among the different envisaged textures, nanocrystalline ceramics are dense materials (relative density above 90%) with mean grain size below 100 nm. From a mechanical point of view, micrometre-grained ceramics are typically brittle, whereas nanometre-grained ceramics have a singular ability to undergo important elongation before breaking at moderate temperatures (i.e. at temperatures around half a ceramic's melting point). The mechanism of deformation in these nanocrystalline ceramics is thought to be superplastic deformation [2].

Ceramics processing is a fundamental technological issue, which has been studied experimentally for many years. However, the mechanisms of sintering have not been totally clarified, especially at the nanometric scale, and the phenomenological equations in the literature are not always backed by theoretical considerations. The laws of sintering depend on different parameters, such as temperature, pressure, grain size and doping. The synthesis of dense nanocrystalline ceramics generally uses pressure-assisted sintering techniques to preserve the grain size. The high densification rate observed at low temperature under pressure can be explained by superplastic deformation that allows the closing of large pores [2]. The process of superplastic deformation is envisaged as grains or groups of grains sliding past each other to take up new positions in the deforming solid. Of course, nanosized particles facilitate this mechanism.

The objective of our work is a better understanding of the mechanisms playing a role in the sintering of TiO_2 anatase nanoparticles. The anatase phase is metastable at reduced temperature and seems to be stabilized at low grain size, due to a small surface energy [3]. Several publications treat the problem of the sintering of TiO_2 nanoparticles to obtain dense rutile [4], [5] and [6], two-phase anatase–rutile [7], [8] and [9] or pure anatase nanoceramics [10]. In the following, we report dilatometric experiments on the hot compaction of anatase nanopowders. Dilatometric analysis allows the determination of the sintering mechanisms. The sintering dynamics can be investigated using the so-called constant rate of heating (CRH) method [11], which allows the determination of an effective activation energy of the densification process.

We report the study of pressure-assisted densification of nanopowders as a function of particle size from 12 to 70 nm and also using different dopants (0.1–1 mol%): Zn^{2+}, Al^{3+}, Si^{4+}, Nb^{5+}. The dopant cations have different charge and radius and may segregate to boundaries due to electrostatic or mechanical driving forces. The crystallographic position and distribution of dopant ions were studied by extended X-ray absorption fine-structure spectroscopy (EXAFS) [12] or secondary ion mass spectroscopy (SIMS) [13], respectively. Whereas donor-type Nb^{5+} (r_{ion} = 69 pm [14]) is dissolved on bulk substitutional Ti^{4+} sites (r_{ion} = 68 pm [14]), the other dopants segregate at grain boundaries at larger concentrations, due to space charge effects for acceptor cations (Zn^{2+}, r_{ion} = 74 pm; Al^{3+}, r_{ion} = 51 pm [14]) and mechanical effects for undersized Si^{4+} (r_{ion} = 42 pm [14]) and Al^{3+} ions. In the latter cases, dopant segregation to the boundary core is expected. Particle size effects on the sintering mechanism as well as acceptor and donor effects on anatase defect chemistry, and mechanical effects due to segregated boundary layers are considered in the following.

2. Experimental

The anatase powders were prepared by the sulphate route [15]. In this process, the mineral precursor is dissolved in sulphuric acid and the titanium sulphate solution then hydrolyzed by heating to 95–110 °C. The hydrolysis product is filtered and the filtrate thoroughly washed until neutral pH is obtained. It is then calcined under air for 1 h at temperatures between 300 and 800 °C to obtain a well-defined particle size distribution. Samples calcined at 300, 600, 700, and 800 °C are particularly considered in the following and are called samples A, B, C and D respectively.

The powders obtained were chemically analysed by gravimetric techniques and inductively coupled plasma emission analysis [15]. The doped samples (Zn, Al, Si, Nb) were prepared by adding a defined concentration (0.1, 0.4 and 1 mol%) of a metal cation salt to the titanium sulphate solution prior to precipitation. Mean particle sizes were determined by correlation of three experimental methods: X-ray diffraction (XRD), transmission electron microscopy (TEM) and nitrogen adsorption measurements using the Brunauer–Emmett–Teller technique (BET) [16].

The hot press used was a prototype built in collaboration with Cyberstar, Grenoble [17]. It permits densifying under a load of up to 5000 kg at temperatures up to 1100 °C. The dies were of pure alumina with internal diameters of 4 mm (SOTIMI, Grez-le-Loing). The

apparatus was equipped with a digital comparator with ±1 μm precision (Sylvac S229), which allows dilatometric measurements. The measured experimental value during dilatometric experiments is the shrinkage $\Delta l(t)$ of the sample. For uniaxial hot compaction, the shrinkage is related to the relative density ρ by the equation [18]

$$\rho(t) = \frac{\left(1 - \frac{(l_i - l_f)}{l_i}\right)}{\left(1 - \frac{\Delta l(t)}{l_i}\right)} \rho_f = \frac{\rho_f l_f}{(l_i - \Delta l(t))} \quad (1)$$

where l_i and l_f are, respectively, the initial and final thickness of the sample pellet and ρ_f is the final relative density, which can be calculated using the mass and geometrical dimensions of the sintered pellet and the theoretical density of the material. The procedure is to apply first a constant pressure (here in general P = 0.44 GPa) and then to increase temperature with a programmed rate of 5 or 1 °C/min. The real sample temperature is measured using a 30% Pt–Rh/6% Pt–Rh thermocouple; the real heating rates were 4.7 or 1.0 °C/min, respectively. After reaching the desired temperature, the sample was held at this plateau for 2 h or directly cooled. The experiments were carried out in air. The microstructures of the ceramics were observed using scanning electron microscopy (SEM) and transmission electron microscopy (TEM). SEM experiments (Philips XL30 SFEG) were carried out on a chip of ceramic in secondary electron mode at 10–15 kV acceleration voltage. TEM experiments (JEOL 2010 F) were realized at 200 kV on a 15 × 5 × 0.1 μm thin blade obtained by focused ion beam (Philips FIB 200) cutting (CP2M, Marseille).

High-pressure experiments were performed using a membrane diamond anvil cell (MDAC) [19] with a diamond tip of diameter 600 μm, allowing pressure on the sample as high as 10 GPa and direct optical observation of the compression through the diamond. After the T301 steel foil gasket had been pre-indented to 40 μm from a starting thickness of 250 μm, TiO_2 powder A was loaded into a chamber of 300 μm in diameter that had been spark eroded in the centre of the pre-indentation. The pressure inside the chamber was monitored by the shift of the $^2F_g \rightarrow {}^4A_{2g}$ fluorescence bands of Cr^{3+} ions in a small ruby crystal placed in the vicinity of the sample [20] and [21]. We checked that the compressed sample still had an anatase structure for the whole pressure range investigated, using Raman spectra recorded in backscattering geometry with a Dilor XY multichannel spectrometer equipped with a 20 slwd-microscope objective. The 514.5 nm line of an Ar^+ ion laser was used as the excitation line.

3. Results and discussion

At temperatures below 400 °C, densification is observed only above 100 MPa [22]. To be efficient, the applied pressure during hot pressing has to be greater than the internal stress of

the nanoparticles. To a first approximation, the sintering stress σ can be expressed as a function of the mean specific surface energy γ of the material and mean pore radius r_p by

$$\sigma = \frac{-2\gamma}{r_p} \quad (2)$$

Using an experimental value of γ for the anatase phase (0.4 ± 0.1 J m^{-2}) [3] and a typical pore size for our samples ($r_p \approx 10$ nm [16]), one obtains a typical sintering stress of 80 MPa which is in good agreement with our observations.

3.1. Influence of particle size

The sintering behaviour of a powder, such as the maximum shrinkage rate and the final density achieved, is influenced by the mean particle size and the extent of hard agglomeration. We have previously determined the particle size distribution of anatase precursor powders A–D [16]. The mean particle sizes and standard deviations are reported in Table 1. Particle agglomeration makes this determination non-trivial, especially for the smallest sizes. Fig. 1 shows the densification rate plotted versus sintering time, $d\rho/dt = f(t)$, for sample powders A–D. A first small shrinkage peak (2–3% of total shrinkage) around 100 °C is observed for all samples. According to Das and Kausik [23], this could correspond to elimination of physisorbed water. To verify this hypothesis, we plot the mass loss determined by thermogravimetry between 25 and 200 °C and the peak maximum vs. particle size (Fig. 2). There is a clear correlation between both data; water desorption might allow a spatial reorganization of particles with easier gliding. Furthermore, the curve for sample A shows a shoulder between 200 and 300 °C, which we attribute to grain growth, given that powder sample A was calcined at the lowest temperature, i.e. 300 °C. Finally, the maximum densification rate $(d\rho/dt)_{max}$ for each sample (Table 1) decreases strongly when the mean particle size increases. A double logarithmic plot of maximum densification rate obtained at 490 °C vs. inverse average particle size is presented in Fig. 3. We notice that the values for powder A and B are identical, which is probably due to grain growth in the case of sample A during hot pressing, as mentioned above.

Table 1.

Maximum densification rate and final density at 490 °C, and effective activation energy as a function of particle size

Sample	Particle size (nm)	Maximum rate (±0.05 min^{-1})	ρ_f (±2%)	nE_a (eV)
A	12 ± 3	0.72	91	0.12
B	24 ± 10	0.72	91	0.24
C	35 ± 15	0.59	85	0.29
D	70 ± 35	0.25	78	0.40

Experimental conditions: 0.44 GPa; plateau: 2 h at 490 °C.

Fig. 1. Densification rate for different powder particle sizes (A = 12 nm, B = 24 nm, C = 35 nm and D = 70 nm). The temperature evolution is given by the solid line.

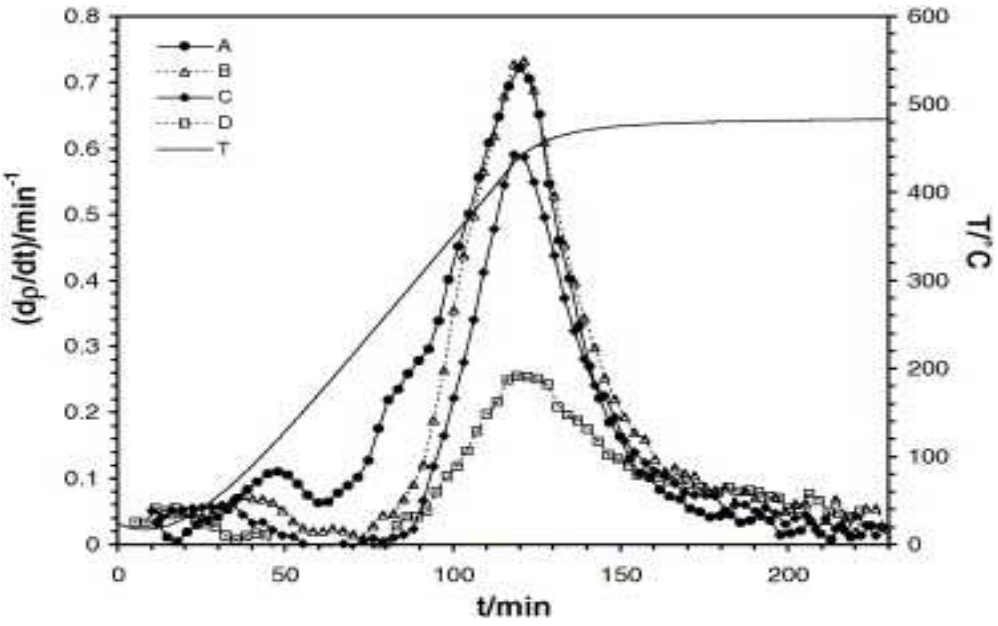

Fig. 2. Maximum densification rate (first peak) and mass loss as a function of particle size.

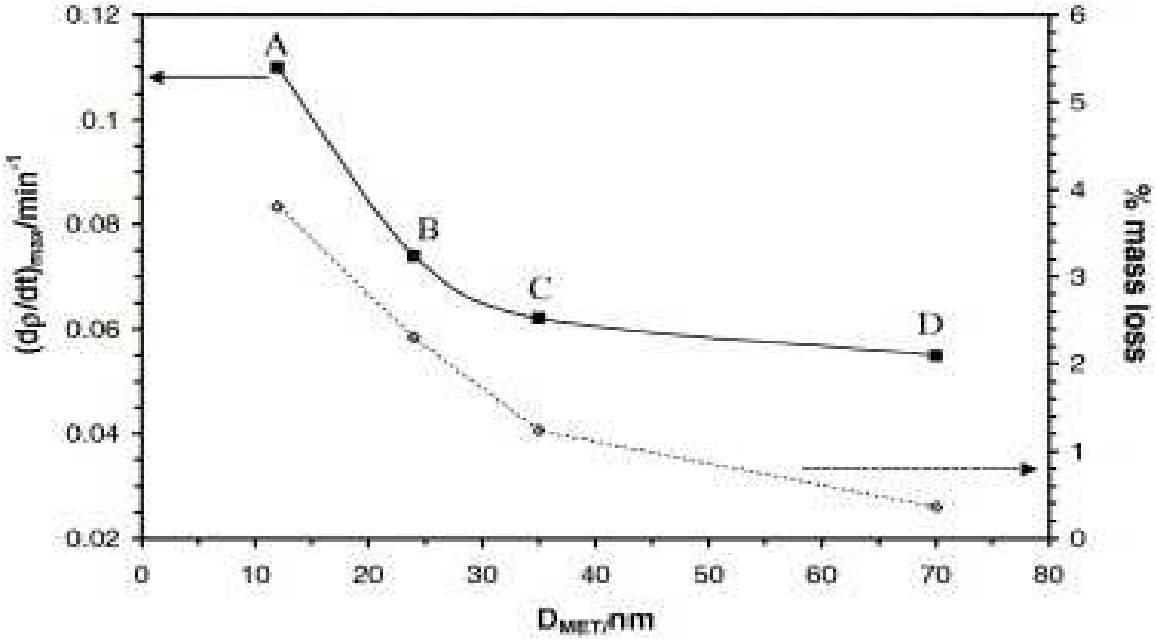

Fig. 3. Maximum densification rate as a function of inverse particle size at 490 °C and t = 2 h.

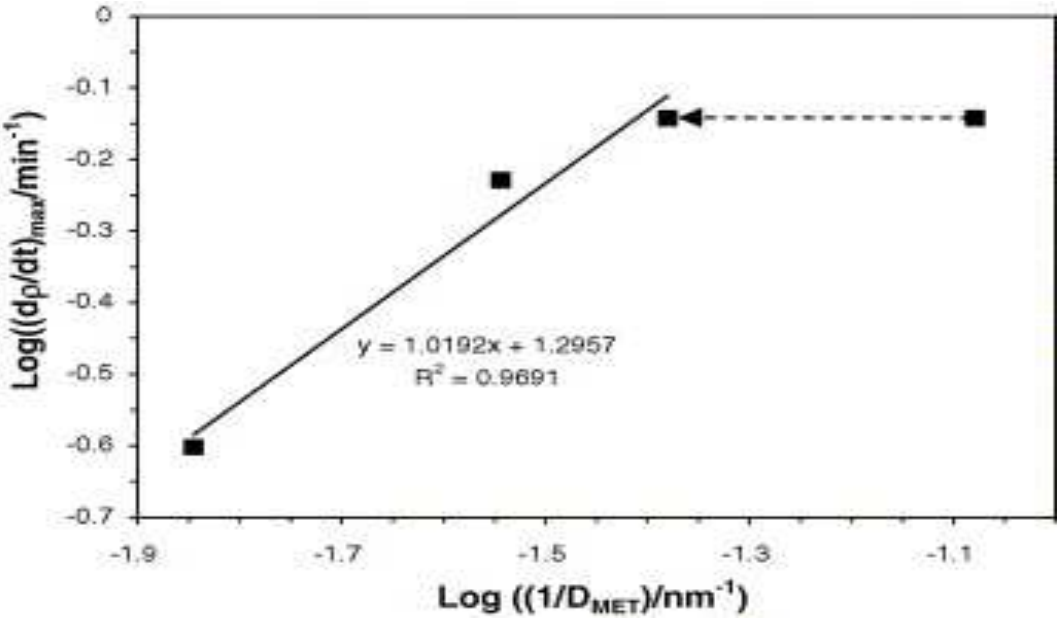

The dependence of pressure (P) and particle radius (r) on densification rate is classically described according to the equation [24]

$$\left(\frac{d\rho}{dt}\right)_T = \frac{KP^n}{r^n} \tag{3}$$

The power n at constant temperature and pressure, which is related to the predominant densification mechanism, can be calculated from the plots in Fig. 3: we obtain $n \approx 1$. However, sintering is observed in our work under uniaxial pressure and shrinkage is not uniform in the axial and radial directions. To compare with literature results using isostatic conditions, we have to derive the equivalence between our one-dimensional shrinkage $l_{1D}(t)$ and a three-dimensional shrinkage $l_{3D}(t)$:

$$\rho_{3D}(t) = \frac{m}{V} = \frac{m}{l_{3D}^3(t)} \qquad \rho_{1D}(t) = \frac{m}{V} = \frac{4m}{\pi\varphi^2 l_{1D}(t)} \tag{4}$$

where φ is the pellet (and die) diameter. Assuming $l_{3D}(t) = l_{1D}(t)$, one can deduce

$$\rho_{1D}(t) = \rho_{3D}^{1/3}(t)\frac{4m^{2/3}}{\pi\varphi^2} \tag{5}$$

$$\left(\frac{d\rho_{1D}}{dt}\right)_T = \frac{K' P^{n/3}}{\rho^{n/3}} \tag{6}$$

Using this hypothesis, one obtains for the granulometric exponent $n_{3D} = 3n_{1D} = 3$, which corresponds to a grain boundary diffusion mechanism at 490 °C under 0.44 GPa.

The densification rate is plotted in Fig. 4 for samples A–D, but now up to 615 °C without a plateau. It is very clear from this graph that on decreasing the particle size, the temperature of maximum shrinkage is shifted to lower values, i.e. ΔT = 160 °C between 12 and 70 nm, while the maximum shrinkage rate is similar for all particle sizes. Typical SEM and TEM images of nanocrystalline ceramics prepared from precursor powders with the two extreme particle sizes are shown in Fig. 5 and Fig. 6. These images confirm the high density of the samples and the absence of significant grain growth during hot pressing.

Fig. 4. Densification rate for different particle sizes between 25 and 615 °C. The temperature evolution is given by the solid line (no plateau).

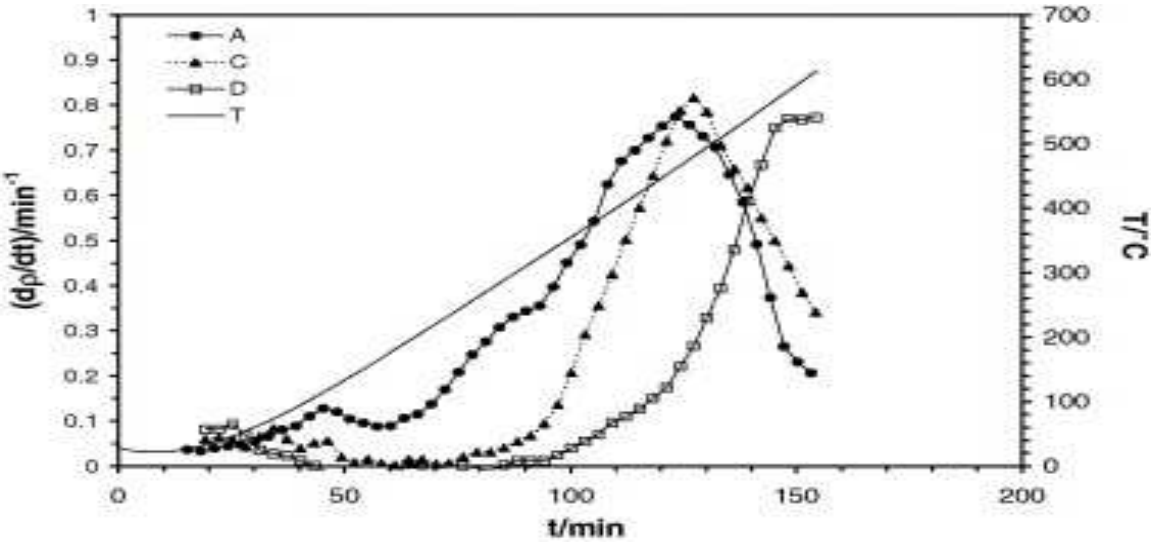

Fig. 5. Representative SEM micrographs of a dense ceramic obtained with precursor D (average particle size = 70 nm).

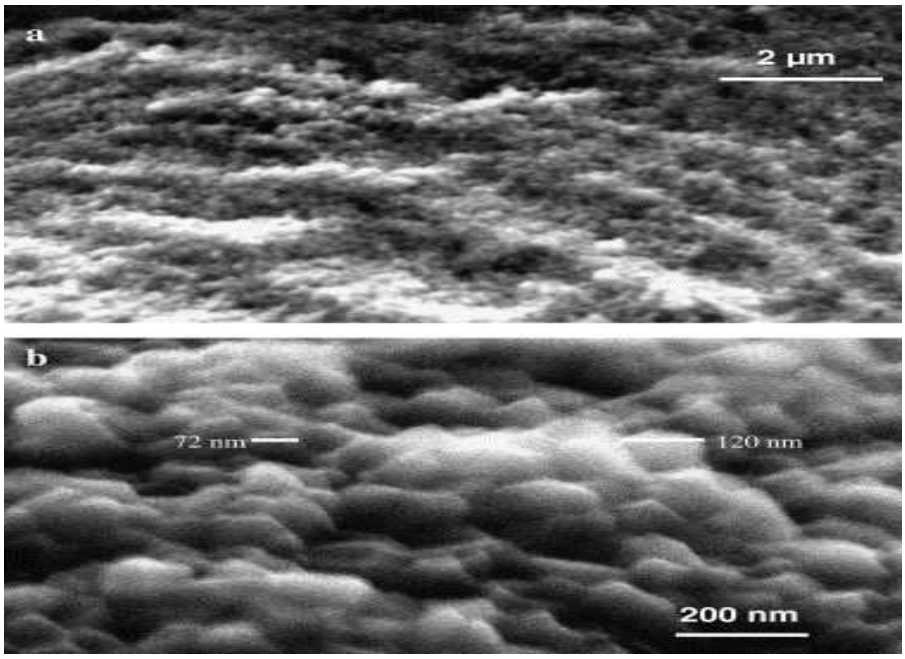

Fig. 6. Representative TEM micrograph of a dense ceramic obtained with precursor A (average particle size = 12 nm).

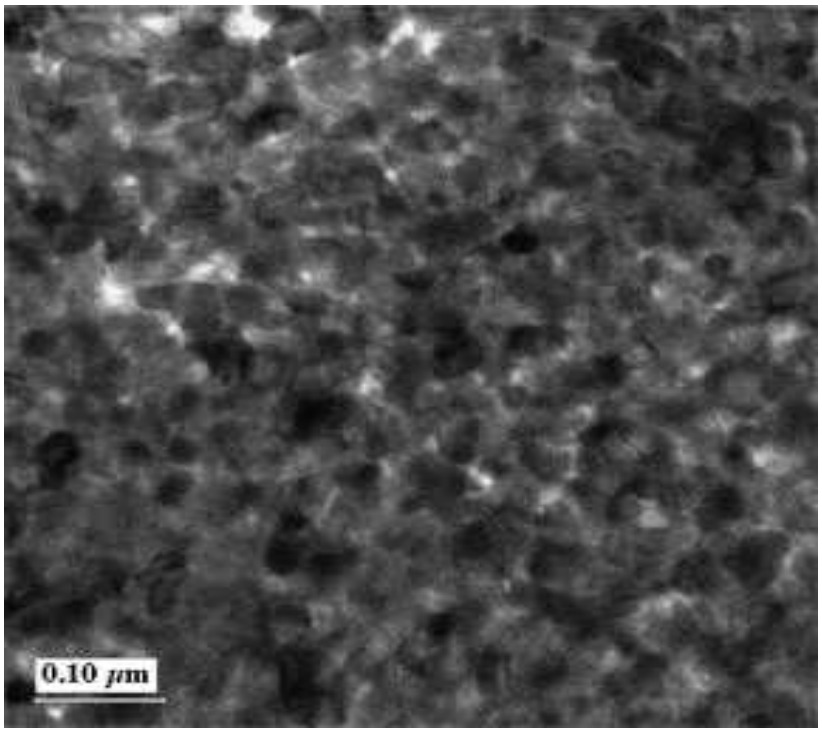

3.2. Effective activation energies

The CRH method [11] allows the determination of an effective activation energy of the predominant densification process. The CRH method is based on a theoretical sintering model of spherical particles by diffusion [25] and [26]. This method is useful only during elimination of open porosity in the sample, but cannot be applied for the last sintering stage corresponding to removal of closed pores, because the mechanisms are here more intricate [18]. The following expression can be derived for predominant grain boundary diffusion:

$$T\left(\frac{\Delta l}{l_i}\right)^{2.06}\frac{d(\Delta l/l_i)}{dT}=\frac{0.7\gamma\Omega d D_{GB}}{kr^4 c} \tag{7}$$

where c is the constant heating rate, γ the surface energy, r the particle radius, and Ω, D_{GB} and d the free volume, diffusion coefficient and thickness of the grain boundary, respectively. Using $dD_{GB} = D_{0,GB}\exp(-E_a/RT)$, where E_a is the activation energy and R the gas constant, one obtains after integration

$$\frac{\Delta l}{l_i}\frac{1}{\sqrt[3]{T}}\approx\left(\frac{2.14\gamma\Omega D_{0,GB}R}{kr^4 cE_a}\right)^{1/3}\exp\left(-\frac{E_a}{3RT}\right) \tag{8}$$

In principle, an effective activation energy $E_a/3$ can be calculated from a plot of $\log[\Delta l/(l_i T^{1/3})]$ versus $1/T$ for predominant grain boundary diffusion. This activation energy should be

independent of the heating rate c. Considering the small influence of temperature in the logarithmic term, a simple plot of $\log[\Delta l/(l_i T)]$ vs. $1/T$ was used by Young and Cutler and is used in the following.

To verify the validity of the CRH method in the case of hot pressing, we checked the independence of the effective activation energy on heating rate for the precursor A at programmed rates of 1 and 5 °C/min (Fig. 7(a)). The difference between the values is only about 10%, which implies that the CRH model can be applied for densification under pressure. Effective activation energies determined by the CRH method for different samples are shown in Fig. 7(b). A constant slope is observed in the case of sample A, whereas a change of activation energy appears for the larger particles, indicating a change of sintering mechanism. The sintering of 12 nm particles is thus governed by a unique process with an effective small average activation energy of 0.12 eV. For larger particles B–D, the intermediate-temperature mechanism is identical to that for sample A, but at higher temperature, between 350 and 450 °C, a second mechanism predominates with larger effective activation energy, increasing from 0.24 for 24 nm particle size to 0.40 eV for 70 nm particles size. At low temperature, no shrinkage is observed, probably due to a combination of size effect and more rigid agglomerates (“pre-sintered” precursor powders).

Fig. 7. (a) Verification of CRH model at two heating rates for powder A. (b) CRH plot for different particle sizes between 25 and 615 °C.

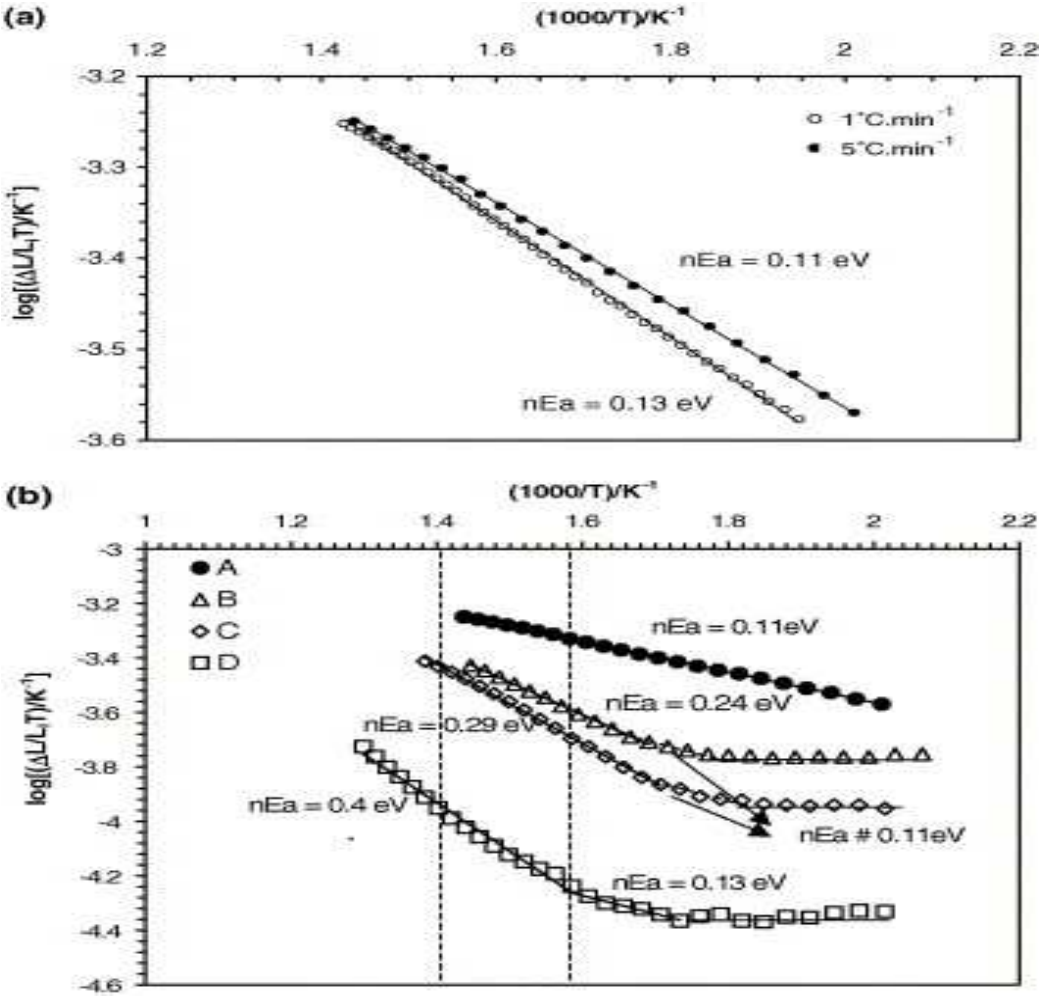

To differentiate the two mechanisms, the influence of pressure on activation energies was investigated for two extreme particle sizes (12 and 70 nm). The variation of effective activation energy is negligible for small grains (Fig. 8(a)), indicating a mechanism without classic diffusion, such as superplastic deformation, reported for nanocrystalline materials including TiO_2 [27]. For larger particles (Fig. 8(b)), the activation energy for the low-temperature part is also independent, but that of the higher temperature mechanism increases, as expected, with pressure from 0.3 to 0.4 eV, indicating grain boundary diffusion. For the diffusion part, the activation energy obtained from Eq. (8) (3×0.4 eV = 1.2 eV) is near literature values for surface diffusion in TiO_2 (1 eV [28]) and in CuBr–TiO_2 composites (1.0 eV [13]), but clearly below that reported for grain boundary diffusion of oxygen vacancies (2.2 eV [29]). In general, surface diffusion does not cause significant densification in the case of pressureless sintering, but one might argue about the pressure effect on surface diffusion. Indeed, the combination of pressure and surface diffusion could permit significant

shrinkage. In the absence of sufficient evidence, we will speak in the following more generally of “boundary” diffusion.

Fig. 8. Influence of pressure on activation energies for two extreme particle sizes: (a) powder A and (b) powder D.

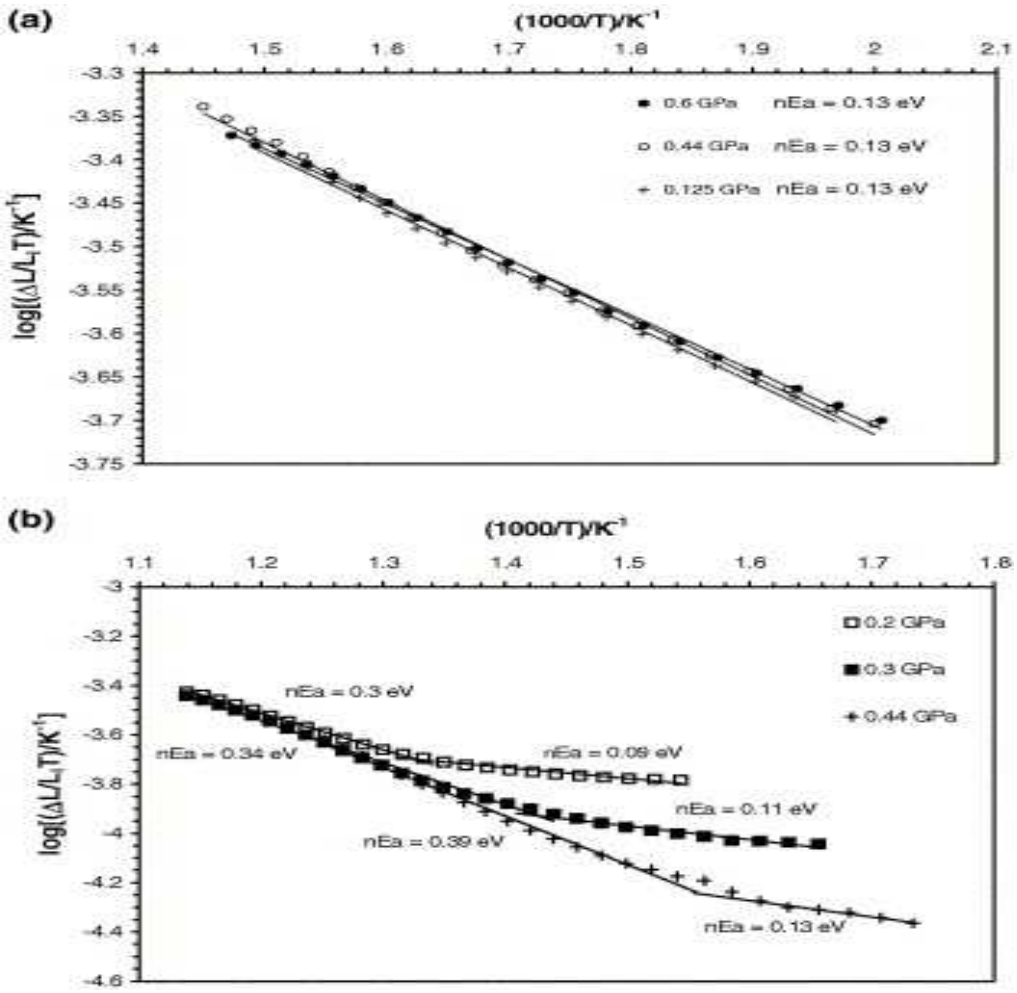

To go deeper into the analysis of densification assisted by “plastic” deformation, we present preliminary high-pressure experiments on batch A. Optical micrographs of nanocrystalline anatase ceramics prepared by cold compaction under high applied pressure in the MDAC at room temperature are shown in Fig. 9. With increasing applied pressure up to 3.3 GPa, we observed a gradual enhancement of the optical transparency of the ceramic (Fig. 9(a), (b) and (d)). At 3.3 GPa, the ceramic is highly dense with minor pores (Fig. 9(e)), although no high-temperature treatment was applied and diffusion can be neglected here. Raman spectra

demonstrate that the ceramic is still of pure anatase structure, in agreement with recent publications that have concluded that the reduction of size increases the pressure range of stability of the anatase structure [30], [31] and [32]. Moreover, the slope measured for the pressure dependence of the most intense Raman modes E_g of nanocrystalline anatase at 145 cm^{-1}, i.e. 2.52(4) cm^{-1}/GPa (between ambient pressure and 15 GPa) is consistent with the enhanced bulk modulus values observed with reduction of size (35% higher than the microcrystalline counterpart) [30] and [33]. With such high values for bulk modulus, we might expect that individual nanograins are hardly compressible; the densification of the ceramic must occur at a scale smaller that the average light diffusion wavelength (600 nm) to explain the perfect transparency of the ceramic. Even if the applied pressure is higher than in the hot-pressing experiments, these results and the activation energy reported above are strong arguments for a densification at reduced temperature due to superplastic deformation.

Fig. 9. Optical micrographs of nanocrystalline anatase ceramics prepared in the MDAC at ambient temperature under different pressures: (a) 0.6 GPa, (b, c) 1.2 GPa, (d, e) 3.3 GPa. Images (a), (b) and (d) are recorded with light coming from both under and above the ceramic

whereas images (c) and (e) are recorded with light coming only from under the ceramic. The ruby crystal used to calibrate the pressure is clearly seen on the right bottom of the ceramic.

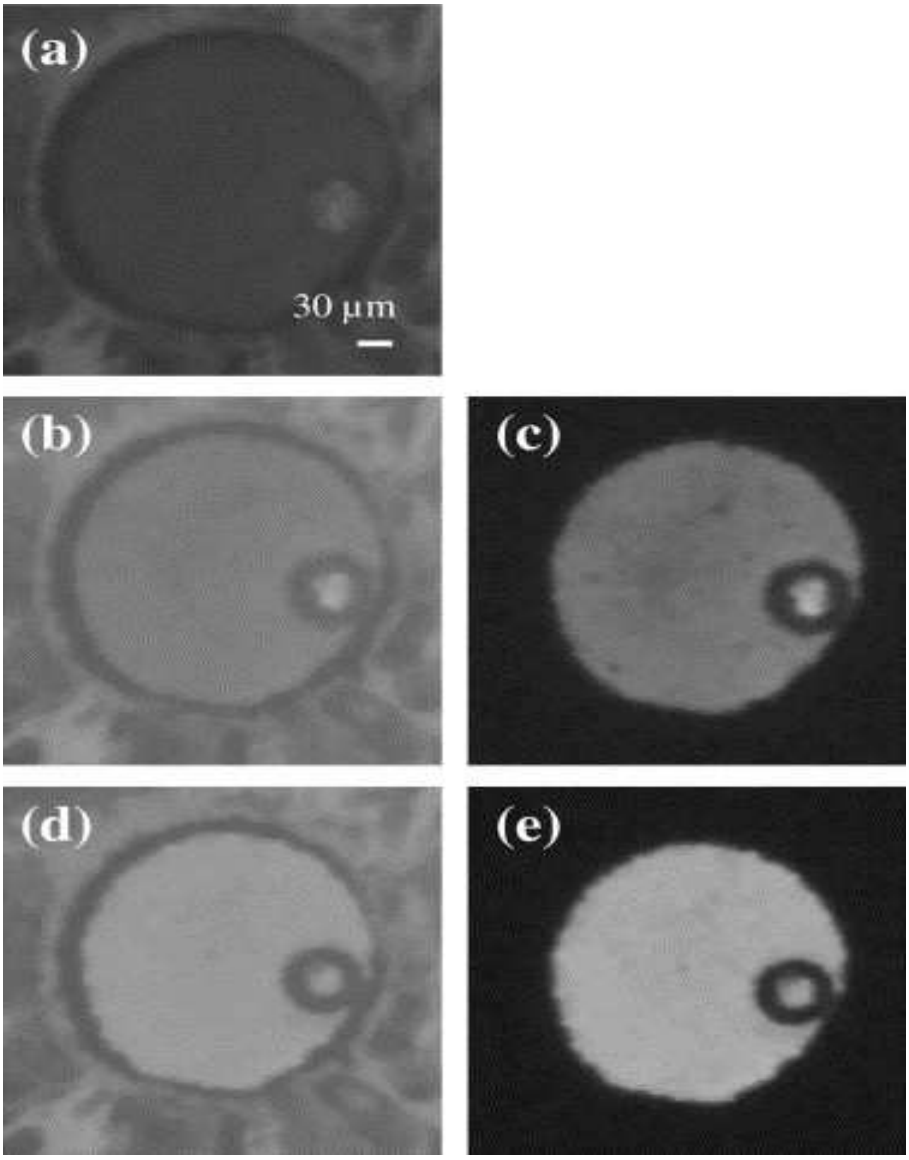

3.3. Influence of doping

All the experiments presented were carried out using the same precursor powder B at P = 0.44 GPa, T = 490 °C and t = 2 h. For Nb, samples with different Nb concentrations have comparable densification rates (Fig. 10(a)). The maximum densification rate is higher than that of nominally undoped samples (Table 2), but the activation energy determined by the CRH method (Fig. 10(b)) is comparable. For Zn, the maximum densification rate is comparable to the Nb case for moderate concentrations, but distinctly higher for 1 mol% (Fig. 11(a) and Table 2). The activation energy measured by the CRH method (Fig. 11(b)) is similar to the undoped value. Densification rates with comparable concentrations (≈ 0.4 mol%) of Zn, Nb, Si, and Al dopants are presented in Fig. 12(a). The rates are distinctly lower for Si- and Al-doped samples. The apparent activation energies (Fig. 12(b)) are similar to the undoped case for all dopants, except for Si, which gives a clearly larger value.

Fig. 10. Influence of Nb concentration on (a) densification rate (the heat treatment is given by the solid line) and (b) CRH plot.

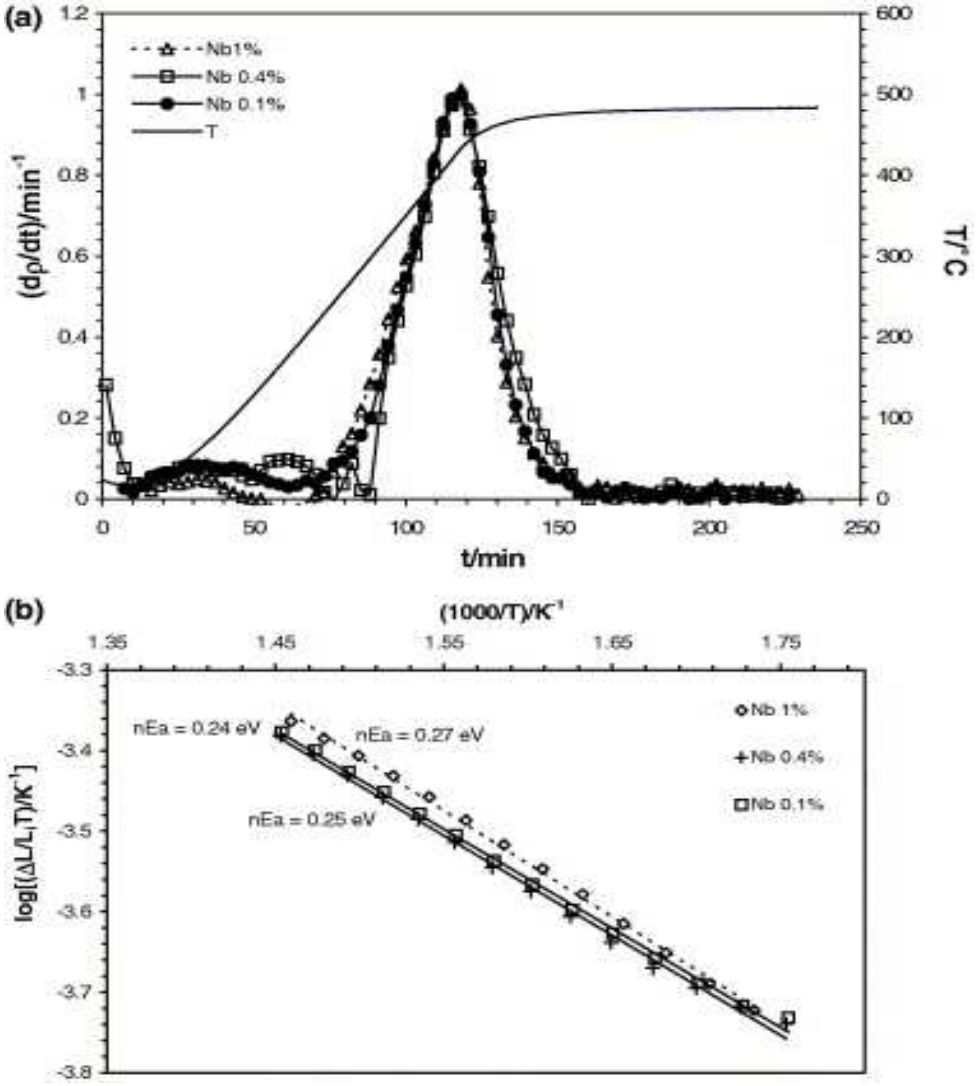

Table 2.

Maximum densification rates and final densities at 490 °C, and effective activation energies for pure and doped anatase ceramics

Dopant	**Concentration (mol%)**	**Maximum rate (±0.05 min^{-1})**	**ρ_f (±2%)**	**nE_a (eV)**
Undoped	–	0.72	91	0.24
Zn^{2+}	0.11	0.9	91	0.23
	0.47	0.9	91	0.28
	1	1.2	91	0.28

Dopant	Concentration (mol%)	Maximum rate (±0.05 min^{-1})	ρ_f (±2%)	nE_a (eV)
Nb^{5+}	0.1	1.0	91	0.25
	0.4	1.0	91	0.24
	1	1.0	91	0.27
Si^{4+}	0.4	0.5	78	0.45
Al^{3+}	0.47	0.55	81	0.23

Fig. 11. Influence of Zn concentration on (a) densification rate, and (b) CRH plot. The temperature evolution is given by the solid line.

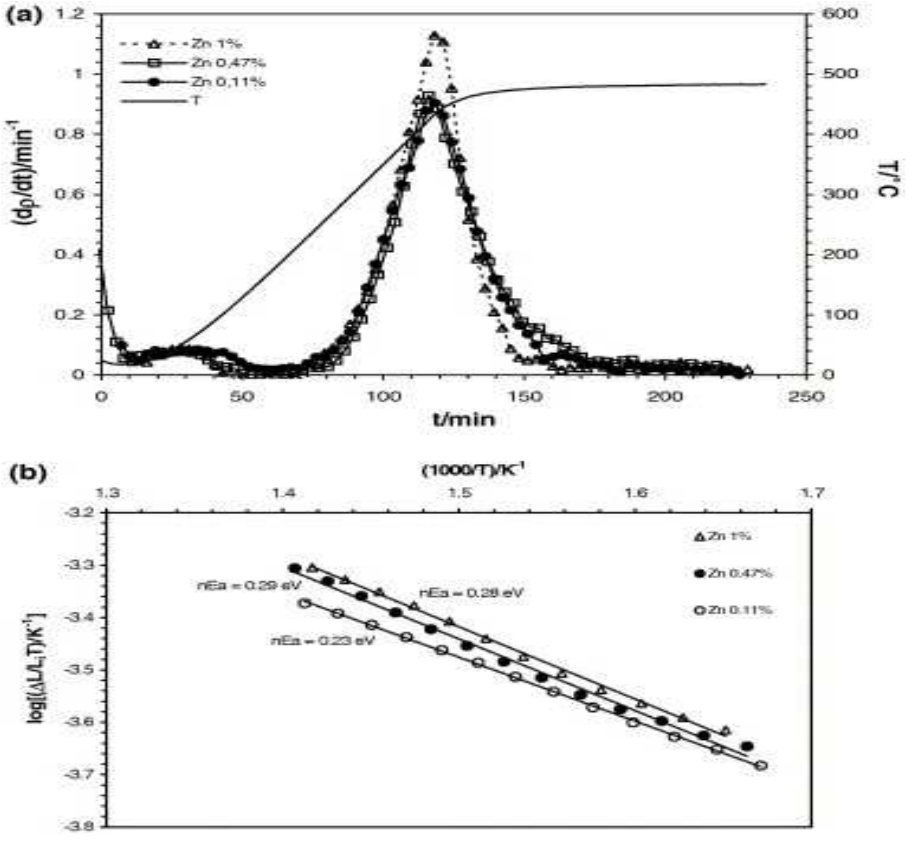

Fig. 12. Influence of different dopants on (a) densification rate, and (b) CRH plot. The temperature evolution is given by the solid line.

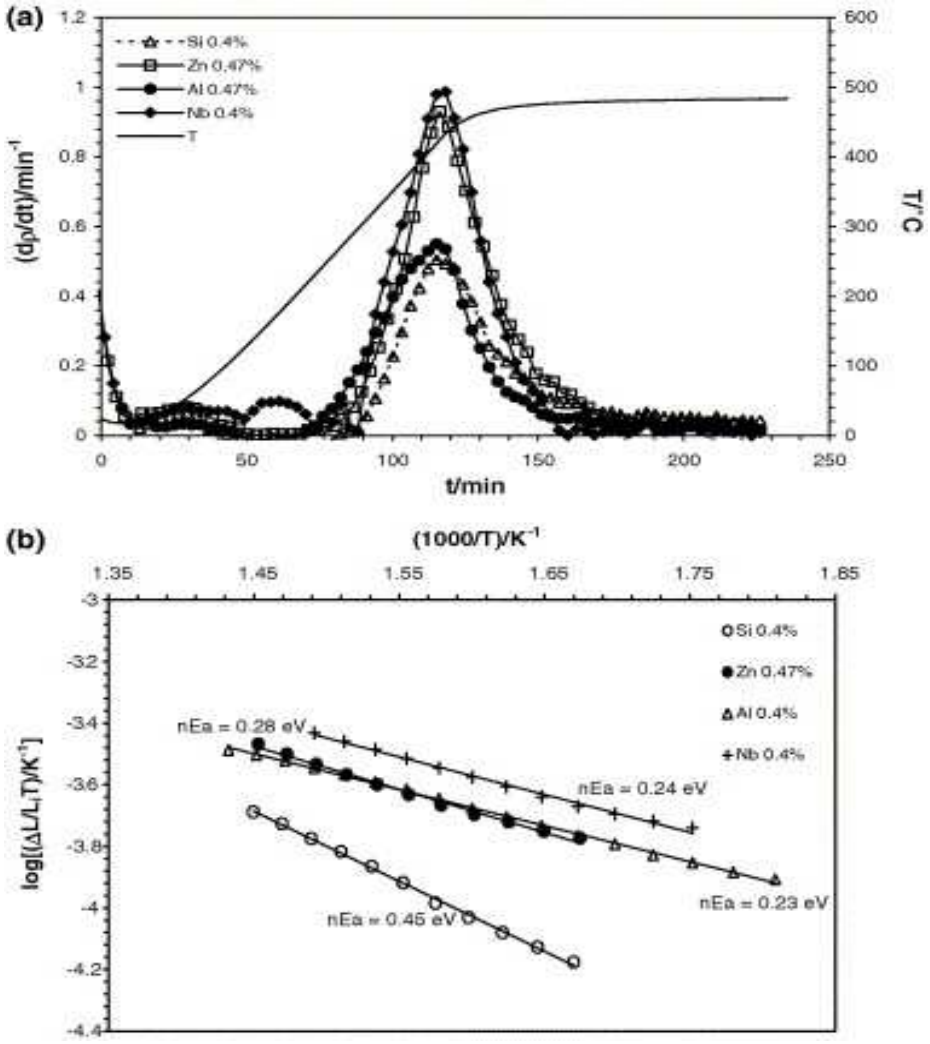

3.4. Defect chemistry

We now discuss the influence of the investigated dopants on defect chemistry and on densification kinetics. Based on Fig. 12(b), it appears that donor doping (Nb) gives the highest densification rates. Acceptor doping (Zn, Al) gives very similar but somewhat smaller rates and isovalent Si has clearly a detrimental effect on densification. The apparent activation energies are similar to the undoped case, except for Si where it is clearly enhanced.

As shown previously using $P(O_2)$-dependent electrical conductivity measurements, anatase shows a Schottky-type intrinsic disorder [34] in air and at temperatures below 600 °C, i.e. under the experimental conditions during densification. One can also reasonably assume that

the boundaries are oxygen-deficient, because the energy of formation of Ti ion vacancies is higher than for oxide ion vacancies [35].

Doping effects on densification kinetics can be related to the defect chemistry of the material investigated and its influence on the predominant sintering mechanisms, i.e. in the case discussed here, on superplastic deformation and boundary diffusion.

Superplastic deformation in ceramic materials has been related to high electronic carrier concentration in the bulk or near interfaces, due to insulator–"metallic" transitions or space charge effects [36]. Under high external pressure, e.g. during hot pressing, band overlap of metal cations can lead to enhanced electronic conductivity, allowing enhanced superplastic deformation. Enhanced electronic carrier concentrations in space charge regions can also support superplastic deformation.

Changes of boundary diffusion are expected if the concentration and/or the mobility of ionic defects change. This can be due to boundary core effects or to space charge effects. Considering the relative width of boundary core (typically 0.5 nm; cf. Fisher model of grain boundary diffusion [37]) and space charge regions (up to tens of nanometers at low bulk carrier concentrations [38]), the latter generally play a more important role. The densification rate is normally dominated by the slowest diffusing species and, in anatase, it is usually assumed that oxide ion vacancies are less mobile than Ti ion vacancies.

Among the dopants studied, only Si is isovalent with Ti and no charge compensation is needed. In other words, no improvement of ionic diffusion or superplastic deformation is expected. However, the ion radius of Si is very small. According to segregation theory, considering the large ionic radius difference of Si and Ti and the similar ionic charge, Si is expected to segregate into the boundary core, due to a purely mechanical driving force. The decrease of sintering rate by Si is obvious (Table 2) and can be attributed to a modification of ionic boundary diffusion by oxide ion mobility reduction, due to the presence of segregated Si in the boundary core. This also explains the significant enhancement of apparent activation energy.

The other dopants studied are aliovalent and charge compensation is necessary. Nb is dissolved substitutionally on bulk sites even at 1 mol% [12], according to EXAFS. An ionic

charge compensation by Ti ion vacancies is expected at high oxygen partial pressure [39] and [40], written according to Kröger nomenclature [41] as

$$5Ti_{Ti} + 2Nb_2O_5 = 4Nb'_{Ti} + V''''_{Ti} + 5TiO_2 \quad (9)$$

At low oxygen partial pressures, electronic charge compensation is also possible:

$$2Ti_{Ti} + Nb_2O_5 = 2Nb'_{Ti} + 2\,e' + 2TiO_2 + 1/2O_{2(g)} \quad (10)$$

The improvement of densification rate for all Nb concentrations might indicate a contribution of superplastic deformation, enhanced by supplementary electronic carriers.

Acceptor doping by Zn or Al gives comparable densification rates and activation energies (Fig. 12(b)). Zn dissolves only up to about 0.3 mol% on bulk sites and segregates to the boundaries for larger concentrations, as shown by EXAFS [12]. The ionic charge compensation mechanism for bulk dissolution involves creation of oxygen vacancies:

$$Ti_{Ti} + ZnO + O_O = Zn''_{Ti} + V^{2\bullet}_O + TiO_2 \quad (11)$$

Charge compensation by electron holes is possible only at extremely high oxygen partial pressures, not encountered here. For bulk dissolution of Zn, the sintering rate is intermediate between undoped and Nb-doped samples (Table 2). More remarkable is the large rate enhancement for 1 mol% Zn, where segregation into space charge regions was shown by EXAFS. In this case, the enrichment of Zn acceptors in the space charge region is expected to drag oxide ion vacancies into the space charge region. This might induce a significant enhancement of ionic diffusion, reflected in an increased densification rate.

The case of Al is rather complicated. A mixed segregation mechanism is probable, including electrostatic (Al ions show acceptor-type behaviour) and mechanical contributions (Al ions are much smaller than Ti ions). Furthermore, ordered aluminotitanate compounds exist, such as Al_2TiO_5, and a co-segregation of Al and Ti is predicted in this case. Al clearly segregates to the boundary, as shown by SIMS for the concentrations of this study. The ionic charge compensation mechanism in the bulk can be written as

$$2Ti_{Ti} + Al_2O_3 + O_O = 2Al'_{Ti} + V^{2\bullet}_O + 2TiO_2 \quad (12)$$

Again, charge compensation by electron holes is extremely improbable. The reduction of sintering rate might then be attributable to the presence of segregated undersized Al ions in the boundary core and subsequent reduction of ionic boundary diffusion, as in the Si case. However, effects of the underlying space charge (due to space charge segregation of acceptor Al ions and electrons) might explain that the activation energy is comparable to that for Zn- and Nb-doped samples (Table 2). More work is necessary to understand fully the complex densification process.

4. Conclusion

The sintering mechanism of nanocrystalline anatase appears as a combination of superplastic deformation and boundary diffusion. Whatever the particle size, densification starts by superplastic deformation. For small particles, the maximum densification rate is very high, e.g. above 0.7% of density per minute at temperatures below 500 °C, which indicates a mechanical process for densification rather than diffusion. For intermediate sizes, the effective activation energy increases with particle size from 0.24 to 0.4 eV, indicating a superposition of two mechanisms (superplastic deformation and boundary diffusion). For large particles, boundary diffusion essentially governs the sintering.

Considering the doping experiments, a strong reduction of densification rate is observed for isovalent Si and an increase for Nb donor doping. Acceptor doping by Zn and Al gives intermediate values. Boundary segregation of dopants in the boundary core or space charge regions adjacent to the boundary is an important factor to be taken into account. More work is necessary to reach definitive conclusions.

References

S.C. Tjong and H. Chen, *Mater Sci Eng R* 45 (2004), p. 1.

M.J. Mayo, D.J. Chen and D.C. Hague In: A.S. Edelstein and R.C. Cammarata, Editors, *Nanomaterials: synthesis, properties and applications*, Institute of Physics Publishing, Bristol, UK (1996), p. 191.

A. Navrotsky, *PNAS* 101 (2004), p. 12096.

H. Hahn, J. Logas and R.S. Averback, *J Mater Res* 15 (1990), p. 609.

R.S. Averback, H.J. Höfler, H. Hahn and J. Logas, *Nanostruc Mater* 1 (1992), p. 173.

M. Uchic, H.J. Höfler, W.J. Flick, R. Tao, P. Kurath and R.S. Averback, *Scripta Metall Mater* 26 (1992), p. 791.

C.D. Terwilliger and Y.M. Chiang, *Nanostruc Mater* 2 (1993), p. 37.

H.G. Kim and K.T. Kim, *Acta Mater* 47 (1999), p. 3561.

S.C. Liao, W.E. Mayo and K.D. Pae, *Acta Mater* 45 (1997), p. 4027.

P. Knauth and H.L. Tuller, *J Appl Phys* 85 (1999), p. 897.

W.S. Young and I.B. Cutler, *J Am Ceram Soc* 53 (1970), p. 659.

R. Bouchet, A. Weibel, P. Knauth, G. Mountjoy and A.V. Chadwick, *Chem Mater* 15 (2003), p. 4996.

P. Knauth and G. Auer, *Solid State Ionics* 147 (2002), p. 115.

In: R.C. Weast, Editor, *Handbook of chemistry and physics* (61st ed.), CRC Press, Boca Raton (FL) (1981).

P. Knauth, R. Bouchet, O. Schäf, A. Weibel and G. Auer In: M.-I. Baraton, Editor, *Synthesis, functionalization and surface treatments of nanoparticles*, American Science, Stevenson (CA) (2002).

A. Weibel, R. Bouchet, F. Boulc'h and P. Knauth, *Chem Mater* 17 (2005), p. 2378. A. Weibel, R. Bouchet and P. Knauth, *Mater Res Soc Symp Proc* 756 (2002), p. 193.

D. Lance, F. Valdivieso and P. Goeuriot, *J Eur Ceram Soc* 24 (2004), p. 2749.

R.M. Hazen and R.T. Downs In: R.M. Hazen and R.T. Downs, Editors, *Reviews in mineralogy and geochemistry* 41, Mineralogical Society of America, Washington (DC) (2000).

G.J. Piermarini, S. Block, J.D. Barnett and R.A. Forman, *J Appl Phys* 46 (1975), p. 2774.

H.K. Mao, P.M. Bell, J.W. Shaner and D.J. Steinberg, *J Appl Phys* 49 (1978), p. 3276.

Weibel A, Bouchet R, Denoyel R, Knauth P. J Eur Ceram Soc, submitted for publication.

S.K. Das and D. Kausik, *Thermochim Acta* 406 (2003), p. 199.

D. Bernache-Assolant, M. Soustelle, C. Monty, H. Pastor and J.M. Chaix, Chimie physique du frittage, Hermes, Paris (1993) (p. 264).

J. Frenkel, *J Phys USSR* 9 (1945), p. 385.

D.L. Johnson, *J Appl Phys* 40 (1969), p. 192.

M.J. Mayo, *Nanostruct Mater* 9 (1997), p. 717.

In: A.S. Edelstein and R.C. Cammarata, Editors, *Nanomaterials: synthesis, properties and applications*, Institute of Physics Publishing, Bristol, UK (1996), p. 176.

H.J. Höfler and R.S. Averback, *Mater Res Soc Symp Proc* 286 (1992), p. 9.

V. Swamy, L.S. Dubrovinsky, N.A. Dubrovinskaia, A.S. Simionovici, M. Drakopoulos and V. Dmitriev *et al.*, *Solid State Commun* 125 (2003), p. 111.

G.R. Hearne, J. Zhao, A.M. Dawe, V. Pischedda, M. Maaza and M.K. Nieuwoudt *et al.*, *Phys Rev B* 70 (2004), p. 134102.

V. Swamy, A. Kuznetsov, L.S. Dubrovinsky, R.A. Caruso, D.G. Shchukin and B.C. Muddle, *Phys Rev B* 71 (2005), p. 184302.

T. Arlt, M. Bermejo, M.A. Blanco, L. Gerward, J.Z. Jiang and J. Staun Olsen *et al.*, *Phys Rev B* 61 (2000), p. 14414.

A. Weibel, R. Bouchet and P. Knauth, *Solid State Ion* 177 (2006), p. 229.

K. Ismail, E. Sikora and D.D. Macdonald, *J Electrochem Soc* 145 (1998), p. 3141.

T.J. Davies, A.A. Ogwu, N. Ridley and Z.C. Wang, *Acta Mater* 44 (1996), p. 2373.

Philibert J. Diffusion et transport de matière dans les solides. Editions de Physique Les Ulis; 1987. p. 227.

J. Maier, *Physical chemistry of ionic materials, Ions and electrons in solids*, John Wiley, Chichester, UK (2004).

M. Radecka and M. Rekas, *J Phys Chem Solids* 56 (1995), p. 1031.

J.F. Baumard and E. Tani, *J Chem Phys* 67 (1977), p. 857.

F.A. Kröger, The chemistry of imperfect crystals (second ed.), North-Holland, Amsterdam (1974) p. 2.

Corresponding author. Tel.: +33 491 637 123; fax: +33 491 637 111.

Acta Materialia
Volume 54, Issue 13, August 2006, Pages 3575-3583
Selected Papers from the Meeting “Micromechanics and Microstructure Evolution: Modeling, Simulation and Experiments” held in Madrid/Spain, 11–16 September 2005